

Tubular Curvature Filter: Implicit Pointwise Curvature Calculation Method for Tubular Objects

Elifnur Sunger[†], Beyza Kalkanli[†], Veysi Yildiz, Tales Imbiriba, Peter Campbell, Deniz Erdoğan

Abstract—Curvature estimation methods are important as they capture salient features for various applications in image processing, especially within medical domains where tortuosity of vascular structures is of significant interest. Existing methods based on centerline or skeleton curvature fail to capture curvature gradients across a rotating tubular structure. This paper presents a Tubular Curvature Filter method that locally calculates the acceleration of bundles of curves that traverse along the tubular object parallel to the centerline. This is achieved by examining the directional rate of change in the eigenvectors of the Hessian matrix of a tubular intensity function in space. This method implicitly calculates the local tubular curvature without the need to explicitly segment the tubular object. Experimental results demonstrate that the Tubular Curvature Filter method provides accurate estimates of local curvature at any point inside tubular structures.

Index Terms—Curvature, tubular structure, vascular structure, tortuosity, principal curve, centerline.

I. INTRODUCTION

CURVATURE calculations in images have utility in many application domains, such as object recognition [1], [2], corner detection [3]–[5], face recognition [6], image registration [7], image reconstruction [8], image denoising [9]–[11] and segmentation [12]–[16]. This recognition motivates exploration of curvature calculation methods in image analysis. Image processing literature deals with multiple forms of curvature. This paper deals with the curvature of one-dimensional curves at points along the curve, defined as the reciprocal of the radius of the circle that is tangent to the curve at a specific point. This definition is related to the magnitude of the acceleration vector defined as the second derivative of the tangent vector with respect to the curve length parameter that endows a coordinate system on said curve. Alternate equivalent definitions may inspire different calculation methods [17]. Tubular curvature addressed in this paper addresses the problem of calculating the curvature of

the centerline and other parallel curves contained in a tubular object seen in the image of interest.

This curvature should not be confused with other curvature quantities of interest in image processing, such as the Gauss curvature of an intensity function obtained from the image of such a tubular object, e.g. a vessel, viewed as a two-dimensional surface. Gauss curvature for such a surface is defined as the product of principal curvatures, and is an intrinsic property of the surface [17]. Gauss curvature of such surfaces are commonly employed in image processing [18], but it is not related to the tubular curvature that is under consideration in this paper. Another such curvature definition that is encountered and employed in image processing, but not relevant to the tubular curvature concept is mean curvature. Mean curvature is the average of principal curvatures of a surface and is an extrinsic property of said surface [19]. Various propositions have been made in the literature demonstrating the utility of such measures based on principal curvatures of surfaces extracted from images [1], [20], [21]. For instance, maximum principal curvature is useful for detecting dark edges on a light background, whereas the minimum principal curvature is useful for the reversed intensity situation. Deng et al. [1] use maximum principal curvature images with watershed algorithm to get stable watershed regions for further processing. In Thanh et al. [20], adaptive principal curvature is employed to enhance blood vessel segmentation performance by using both maximum and minimum principal curvature values; the method is empirically shown to perform better than using only one of the principal curvature values, since it improves contrast and brightness of the resulting image. This method employs several derivative operators, such as Sobel derivative operator, Prewitt derivative operator, and derivative by central difference, resulting in high effectiveness on segmentation performance.

In medical application domains, curvature methods based on extracting the centerline are commonly employed model and analyze vascular structures [22]–[24], evaluate severity of disease [25], [26], and design devices [27]. Ciomaga et al. [21] propose the use of vectorial and scalar curvature calculations for visualization of such curvature measures at different resolutions, however this approach requires the extraction of lines from images. Note that these centerline-based curvature assessments may not accurately represent the curvatures differences of tubular objects on the inner and outer sides of a turn.

This paper focuses on tubular curvature calculation by locally calculating the acceleration vectors of tangent vectors to a bundle of curves in the tubular object, parallel to the centerline

[†]Equal Contribution. This work was supported by grants R01 EY019474, and P30 EY10572 from the National Institutes of Health (Bethesda, MD), by unrestricted departmental funding from Research to Prevent Blindness (New York, NY), and the Malcolm Marquis Innovation Fund.

Elifnur Sunger, Beyza Kalkanli, Tales Imbiriba and Deniz Erdoğan are with the Department of Electrical and Computer Engineering, Northeastern University, Boston, MA 02115 USA (e-mail: sunger, kalkanli, talesim, erdogmus@ece.neu.edu). Tales Imbiriba is also with the Institute for Experiential AI, Boston, MA 02115 USA.

Veysi Yildiz is with Identifeye Health, Guilford, CT 06437 USA (e-mail: vyildiz@identifeye.health). Work was done when Veysi Yildiz was with the Department of Electrical and Computer Engineering, Northeastern University.

Peter Campbell is with Department of Ophthalmology, Casey Eye Institute, Oregon Health & Science University, Portland, OR 97239 (e-mail: campbell@ohsu.edu).

that is traced by the ridge of a suitable intensity function that highlights the tubular object. From prior work, these tangent vectors are known to be select eigenvectors of the Hessian of the intensity function. Fig. 1 presents a sample illustration. The method assumes that the image is appropriately preprocessed to yield an intensity image that highlights the tube shaped objects, and is based on interpolating this intensity image to obtain an intensity function over spatial coordinates [2], [20], [21]. The proposed method is referred to as a *Tubular Curvature Filter (TCF)*. TCF involves local calculations on the intensity function and its derivatives, eliminating the need to segment or extract centerlines of tubular objects, unlike centerline-based methods [22]–[28]. The fact that TCF only requires local interpolation and differentiation at points of interest, the method is suitable for parallel processing.

II. METHOD

In this section, the proposed tubular curvature filter concept will be described and a method to compute local tubular curvature at any point for a given thrice continuously differentiable function of Cartesian spatial coordinates in an Euclidean space will be developed. Application to intensity images of tubular shapes will also be discussed.

A. Tubular Curvature

To compute the curvature of tubular shapes over space we exploit the geometrical interpretation of the eigenvalues of the Hessian provided by Ozertem et al. [29]. In Ozertem et al. [29], the authors redefined principal curves and surfaces in terms of first and second derivatives of probability density functions. This definition of the principal curves corresponds to the *ridges* of said probability density function. We motivate our discussion using the example in Fig 1, which presents a discretized image of a function that forms a tubular shape over 2-dimensional (2-D) space; function values are pixel intensities. The *principal curve* that forms the ridge of this function and *parallel curves* traced by select eigenvectors of the Hessian matrix, as defined by Ozertem et al. [29], are represented by the blue-solid and red-dotted lines, respectively. The eigenvectors of the function's Hessian evaluated at a given point are represented by green arrows. It is important to highlight that at any point over the 2-D space, such eigenvectors point toward the principal and to a direction tangential to the parallel curves.

The curvature of parallel curves at any point in space can be defined based on the rate of change of eigenvectors tangent to the parallel curves; for unit-length eigenvectors, this rate of change becomes the acceleration vector. Curvature of these curves at any point is simply the norm of the local acceleration vector. When computing the curvature of tubular structures in an image, an interpolation method will be used to obtain a thrice-continuously differentiable intensity function, from which necessary gradient and Hessian values can be computed for any given point.

Let $\mathbf{x} \in \mathbb{R}^2$ be a point. We define a function $p(\cdot) : \mathbb{R}^2 \rightarrow \mathbb{R}_+^*$ = $\{p(\mathbf{x}) \in \mathbb{R} | p(\mathbf{x}) > 0\}$ as a continuous, positive,

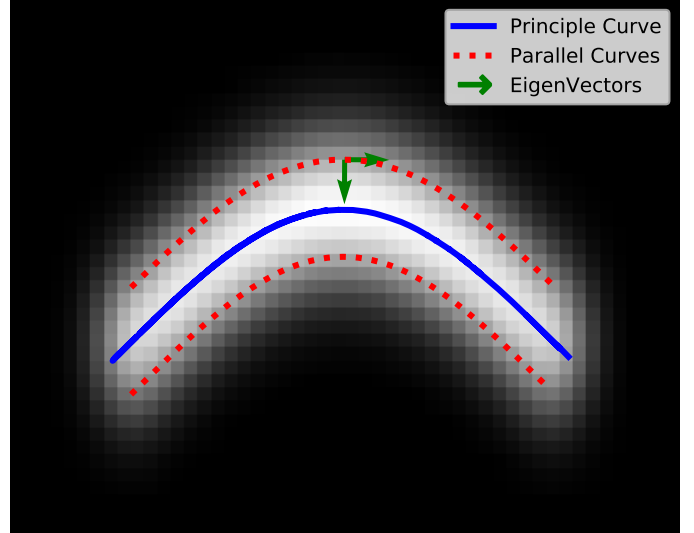


Fig. 1: Example function, its principal curve [29], parallel curves and eigenvectors of Hessian at a sample point.

smooth (thrice differentiable). For images, $p(\cdot)$ can be an interpolated function as explained in Section II-B.

Let $\mathbf{g}(\mathbf{x})$ denote the transpose of the gradient and $\mathbf{H}(\mathbf{x})$ denote the Hessian of the logarithm of the function (see, Appendix A for more details). Let $\{(\lambda_1(\mathbf{x}), \mathbf{q}_1(\mathbf{x})), (\lambda_2(\mathbf{x}), \mathbf{q}_2(\mathbf{x}))\}$ be the eigenvalue-vector pairs of $\mathbf{H}(\mathbf{x})$, and $|\lambda_1(\mathbf{x})| < |\lambda_2(\mathbf{x})|$.

Definition 1. The acceleration vector $\mathbf{a}(\mathbf{x})$, at any point $\mathbf{x} \in \mathbb{R}^2$, is the rate of change of the unit-length \mathbf{q}_1 , which is tangent to the curve, with respect to the curve length parameter s . Using chain rule:

$$\mathbf{a}(\mathbf{x}) = \frac{\partial \mathbf{q}_1(\mathbf{x})}{\partial s} = \frac{\partial \mathbf{q}_1(\mathbf{x})}{\partial \mathbf{x}} \frac{\partial \mathbf{x}}{\partial s}. \quad (1)$$

Since $\mathbf{q}_1(\mathbf{x})$ is the unit length velocity vector, we can write

$$\frac{\partial \mathbf{x}}{\partial s} = \mathbf{q}_1 \text{ as } \partial \mathbf{x} = \mathbf{q}_1 \partial s. \quad (2)$$

Definition 2. Tubular curvature of the intensity function $p(\mathbf{x})$ at point \mathbf{x} is the Euclidean norm of its acceleration vector:

$$c(\mathbf{x}) = \|\mathbf{a}(\mathbf{x})\|, \quad (3)$$

where $c(\mathbf{x})$ is the curvature.

Derivation 1. To calculate the acceleration vector at point \mathbf{x} , the directional derivatives of \mathbf{q}_1 , i.e., $\partial \mathbf{q}_1 / \partial x_1$ and $\partial \mathbf{q}_1 / \partial x_2$, are required; which can be computed using the eigen decomposition of the Hessian matrix. Thus, we decompose $\mathbf{H}(\mathbf{x})$ into its eigenvectors as:

$$\mathbf{H}(\mathbf{x}) = \mathbf{Q}(\mathbf{x}) \mathbf{\Lambda}(\mathbf{x}) \mathbf{Q}(\mathbf{x})^T, \quad (4)$$

where \mathbf{Q} is the 2×2 matrix whose i^{th} column is the eigenvector \mathbf{q}_i , and $\mathbf{\Lambda}$ is diagonal with elements as corresponding eigenvalues. Specifically in the 2-D case:

$$\mathbf{H}(\mathbf{x}) = \begin{bmatrix} \mathbf{q}_1 & \mathbf{q}_2 \end{bmatrix} \begin{bmatrix} \lambda_1 & 0 \\ 0 & \lambda_2 \end{bmatrix} \begin{bmatrix} \mathbf{q}_1 & \mathbf{q}_2 \end{bmatrix}^T. \quad (5)$$

We can calculate $\partial \mathbf{q}_1(\mathbf{x}) / \partial \mathbf{x}$ by taking derivatives of eigen decomposition of Hessian in (5). We define $\mathbf{T}_i(\mathbf{x})$, $\mathbf{V}_i(\mathbf{x})$ and

$\mathbf{L}_i(\mathbf{x})$ as the i^{th} directional derivatives of Hessian $\mathbf{H}(\mathbf{x})$, $\mathbf{Q}(\mathbf{x})$ and $\mathbf{\Lambda}(\mathbf{x})$ respectively:

$$\mathbf{T}_i(\mathbf{x}) = \frac{\partial \mathbf{H}(\mathbf{x})}{\partial x_i} = \begin{bmatrix} t_{i11} & t_{i12} \\ t_{i21} & t_{i22} \end{bmatrix}, \quad (6)$$

$$\mathbf{V}_i(\mathbf{x}) = \frac{\partial \mathbf{Q}(\mathbf{x})}{\partial x_i} = \begin{bmatrix} \frac{\partial \mathbf{q}_1}{\partial x_i} & \frac{\partial \mathbf{q}_2}{\partial x_i} \end{bmatrix} = \begin{bmatrix} v_{i11} & v_{i12} \\ v_{i21} & v_{i22} \end{bmatrix}, \quad (7)$$

$$\mathbf{L}_i(\mathbf{x}) = \begin{bmatrix} \frac{\partial \lambda_1}{\partial x_i} & 0 \\ 0 & \frac{\partial \lambda_2}{\partial x_i} \end{bmatrix} = \begin{bmatrix} l_{i1} & 0 \\ 0 & l_{i2} \end{bmatrix}. \quad (8)$$

\mathbf{T}_i can be written in terms of $\mathbf{Q}(\mathbf{x})$, $\mathbf{\Lambda}(\mathbf{x})$, $\mathbf{V}_i(\mathbf{x})$ and $\mathbf{L}_i(\mathbf{x})$:

$$\mathbf{T}_i(\mathbf{x}) = \mathbf{V}_i(\mathbf{x})\mathbf{\Lambda}(\mathbf{x})\mathbf{Q}(\mathbf{x})^T + \mathbf{Q}(\mathbf{x})\mathbf{L}_i(\mathbf{x})\mathbf{Q}(\mathbf{x})^T + \mathbf{Q}(\mathbf{x})\mathbf{\Lambda}(\mathbf{x})\mathbf{V}_i(\mathbf{x})^T. \quad (9)$$

In this set of equations, the derivatives of eigenvectors and eigenvalues are unknown. Since \mathbf{T}_i matrices are symmetric, we get 3 equations from \mathbf{T}_i . Using two properties of eigenvectors, we obtain additional equations: 1) eigenvectors are unit length; hence, derivatives of their magnitude are zero, and 2) they are perpendicular to each other. With these, we have the following set of additional equations:

$$\frac{\partial \|\mathbf{q}_1(\mathbf{x})\|^2}{\partial x_i} = 2\mathbf{q}_1^T \frac{\partial \mathbf{q}_1}{\partial x_i} = 0, \quad (10)$$

$$\frac{\partial \|\mathbf{q}_2(\mathbf{x})\|^2}{\partial x_i} = 2\mathbf{q}_2^T \frac{\partial \mathbf{q}_2}{\partial x_i} = 0, \quad (11)$$

$$\frac{\partial \mathbf{q}_1^T \mathbf{q}_2}{\partial x_i} = \mathbf{q}_1^T \frac{\partial \mathbf{q}_2}{\partial x_i} + \frac{\partial \mathbf{q}_1^T}{\partial x_i} \mathbf{q}_2 = 0. \quad (12)$$

From \mathbf{T}_i and the properties of eigenvectors, we obtain 6 equations with 12 unknowns. We obtain the following sets of linear equations from (9)-(12):

$$\begin{bmatrix} t_{111} \\ t_{112} \\ t_{122} \\ 0 \\ 0 \\ 0 \end{bmatrix} = \mathbf{M} \begin{bmatrix} v_{111} \\ v_{112} \\ l_{11} \\ l_{12} \\ v_{121} \\ v_{122} \end{bmatrix} \text{ and } \begin{bmatrix} t_{211} \\ t_{212} \\ t_{222} \\ 0 \\ 0 \\ 0 \end{bmatrix} = \mathbf{M} \begin{bmatrix} v_{211} \\ v_{212} \\ l_{21} \\ l_{22} \\ v_{221} \\ v_{222} \end{bmatrix}, \quad (13)$$

where

$$\mathbf{q}_i = [\mathbf{q}_{i1} \quad \mathbf{q}_{i2}]^T, \quad (14)$$

$$\mathbf{M} = \begin{bmatrix} 2\lambda_1 \mathbf{q}_{11} & 2\lambda_2 \mathbf{q}_{21} & \mathbf{q}_{11}^2 & \mathbf{q}_{21}^2 & 0 & 0 \\ \lambda_1 \mathbf{q}_{12} & \lambda_2 \mathbf{q}_{22} & \mathbf{q}_{11} \mathbf{q}_{12} & \mathbf{q}_{21} \mathbf{q}_{22} & \lambda_1 \mathbf{q}_{11} & \lambda_2 \mathbf{q}_{21} \\ 0 & 0 & \mathbf{q}_{12}^2 & \mathbf{q}_{22}^2 & 2\lambda_1 \mathbf{q}_{12} & 2\lambda_2 \mathbf{q}_{22} \\ \mathbf{q}_{11} & 0 & 0 & 0 & \mathbf{q}_{12} & 0 \\ 0 & \mathbf{q}_{21} & 0 & 0 & 0 & \mathbf{q}_{22} \\ \mathbf{q}_{21} & \mathbf{q}_{11} & 0 & 0 & \mathbf{q}_{22} & \mathbf{q}_{12} \end{bmatrix}. \quad (15)$$

We provide the complete derivation of linear equations that leads to \mathbf{M} in Appendix A. Please see Appendix B for derivations of linear equations solved in order to obtain the acceleration vector for functions with n-dimensional arguments, including the 3-D special case (for volumetric images).

By solving the system of linear equations specified above, we can find the elements of $\mathbf{V}(\mathbf{x})$ and $\mathbf{L}(\mathbf{x})$. We can calculate $\frac{\partial \mathbf{q}_1(\mathbf{x})}{\partial \mathbf{x}}$ from $\mathbf{V}(\mathbf{x})$. Finally, we can obtain the acceleration vector at point \mathbf{x} following (1).

B. TCF on Images

The methodology discussed above is designed to operate over continuous thrice differentiable functions defined over \mathbb{R}^2 (and in general \mathbb{R}^n). To apply the TCF to images, we need to smoothly interpolate intensity images to obtain intensity functions with necessary continuity and differentiability properties. This paper does not advocate a particular interpolation methodology. For illustration purposes, in this paper we consider a kernel regression based approach.

Let $\tilde{\mathbf{x}}_j \in \mathbb{Z}_+^2$ and $w_j \in \mathbb{R}_+$, $j \in \{1, \dots, n\}$, represent the location and intensity of the j -th pixel on a image. Then, the kernel-based interpolation is:

$$p(\mathbf{x}) = \sum_{j=1}^n w_j K_{S_j}(\mathbf{x} - \tilde{\mathbf{x}}_j), \quad (16)$$

where $K_{S_j}(\cdot) : \mathbb{R}^2 \rightarrow \mathbb{R}$ is the interpolation kernel with scale matrix S_j .

Variable-scale (width) kernels may be employed in interpolation to achieve robustness against outlier pixel intensities that may arise due to noise or other reasons. The approach outlined in [30] proposes to select k -nearest pixels to \mathbf{x} . For each \mathbf{x} , a sequence $\{\tilde{\mathbf{x}}_{\pi(1)}, \tilde{\mathbf{x}}_{\pi(2)}, \dots, \tilde{\mathbf{x}}_{\pi(n)}\}$ is defined, where $\pi(i) \in \{1, 2, \dots, n\}$ represents the sorted set of pixel indexes such that $\|\mathbf{x} - \tilde{\mathbf{x}}_{\pi(i)}\|_2 \leq \|\mathbf{x} - \tilde{\mathbf{x}}_{\pi(i+1)}\|_2$, and the k -nearest pixels are selected based on this sequence, denoted as $\{\tilde{\mathbf{x}}_{\pi(1)}, \tilde{\mathbf{x}}_{\pi(2)}, \dots, \tilde{\mathbf{x}}_{\pi(k)}\}$, with $k \leq n$. These k -nearest pixels can then be used for kernel-based interpolation:

$$p_\pi(\mathbf{x}) = \sum_{j=1}^k w_{\pi(j)} K_{S_j}(\mathbf{x} - \tilde{\mathbf{x}}_{\pi(j)}). \quad (17)$$

Given the interpolated function $p(\mathbf{x})$, considering that the tubular structure of interest is represented with large function values (high-intensity pixels over a dark background), the application of the TCF is straightforward. The methodology presented in Section II-A was derived, without loss of generality, for images with tubular shapes represented by light pixels over dark backgrounds and use \mathbf{q}_1 for curvature calculations. If tubular objects appear as dark pixels over a light background, the intensity function can be negated to achieve tubular objects with high intensity values.

III. EXPERIMENTAL RESULTS

TCF is applied to artificial and real images in both two and three dimensions. Within this section, we have categorized the results based on the number of dimensions and image type (artificial or real). Gaussian kernels are used in obtaining these results, but other interpolators can be used.

A. Two-Dimensional Results

This subsection consists of two parts. In the first part, we provide curvature results for some artificial images with different curved structures. In the second part, we focus on real-world applications.

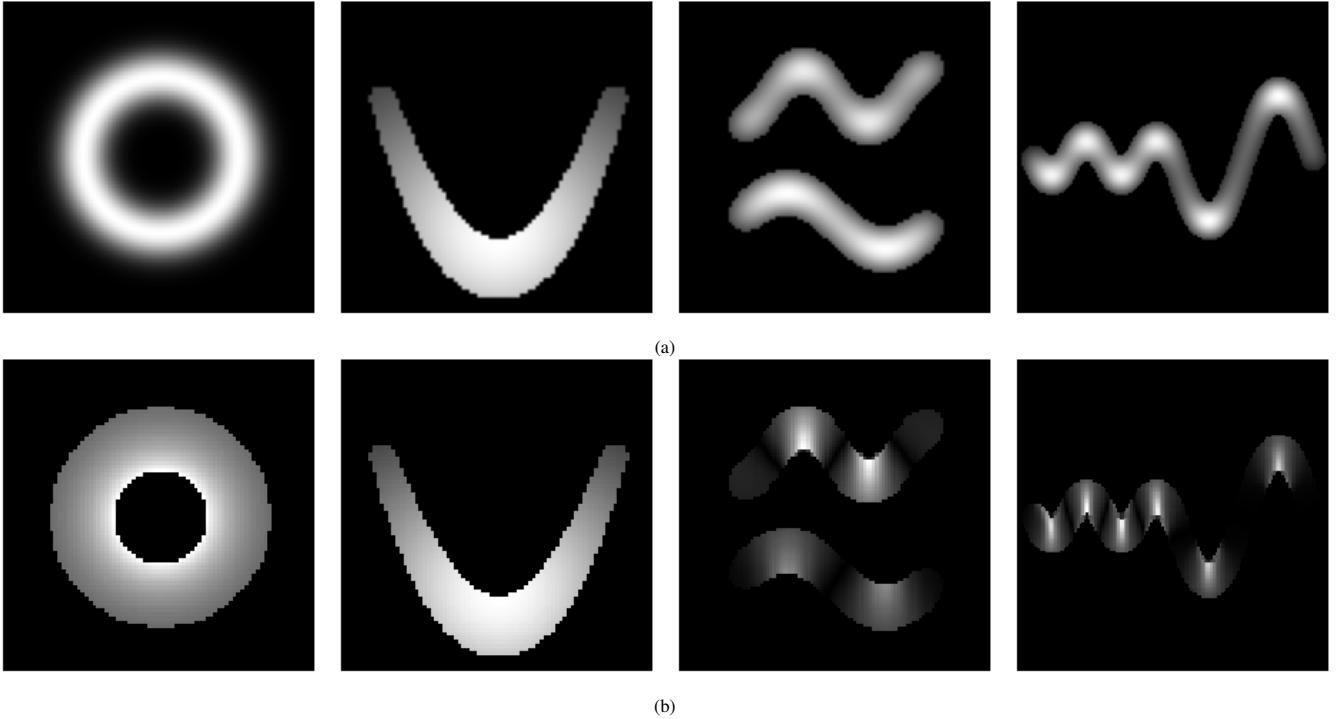


Fig. 2: (a) Blurry ring function $p_{\text{ring}}(\mathbf{x})$, quadratic function $p_{\text{quad}}(\mathbf{x})$, two sine functions with different frequencies $p_{\text{sin},f}(\mathbf{x})$, and a sine function with changing amplitude and frequency $p_{\text{sin},A,f}(\mathbf{x})$ are presented, respectively. (b) The curvature values of the two-dimensional images are calculated using TCF. The intensity values represent the curvature values. Brighter pixels on the curvature plots correspond to higher values.

1) *Artificial Images*: This section presents four different two-dimensional artificial images, including a blurry ring, a quadratic function, two sine waves, and a sine wave with changing amplitude and frequency. Fig. 2 displays these images in the first row, and their corresponding curvature images calculated using TCF are shown in the second row. The intensity values on the curvature images represent curvature values, with brighter pixels corresponding to higher values.

To generate images of the quadratic function, two sine waves, and a sine wave with changing amplitude and frequency, we employ Gaussian kernels as described in (16), with the scale matrix $\mathbf{S}_j = 2\mathbf{I}_2$, where \mathbf{I}_2 represents the two-dimensional identity matrix, and $w_j = 1$ for $j \in \{1, \dots, n\}$. For each of these examples, functions are defined by placing evenly spaced isotropic Gaussian kernels, followed by the creation of images using uniform grids $\mathcal{G}(l, a, b)$ where \mathcal{G} represents a uniform grid with l samples in the interval $[a, b]$.

a) *Image of a Blurry Ring* : We define a blurry ring function $p_{\text{ring}}(\mathbf{x})$ in (18).

$$p_{\text{ring}}(\mathbf{x}) = e^{-(\sqrt{\mathbf{x}^T \mathbf{x}} - r)^2 / m}, \quad (18)$$

where $r = 1$ is the radius of the ring and $m = 0.1$ is the thickness parameter.

The first column in Fig. 2 displays $p_{\text{ring}}(\mathbf{x})$ along with its curvature results. At every point in the ring function, the curvature is reciprocal to the radius of the ring. Consequently, points closer to the center of the ring are expected to exhibit higher curvature values, as demonstrated by TCF.

b) *Image of a Quadratic Function*: We define the quadratic function $p_{\text{quad}}(\mathbf{x})$ by placing equally spaced isotropic

Gaussian kernels along the $y = x^2$ line as in (19).

$$p_{\text{quad}}(\mathbf{x}) = \sum_{j=1}^n K_I(\mathbf{x} - \mathbf{x}_j), \quad (19)$$

where $\mathbf{x}_j \in \{\mathbf{x} = [m, m^2]^T \mid m \in \mathcal{G}(20, -1.5, 1.5)\}$.

The second column of Fig. 2 shows the image of the quadratic function $p_{\text{quad}}(\mathbf{x})$ along with its curvature results. The curvature values for pixels farther from the global minimum of the $y = x^2$ line are smaller, as these regions resemble almost flat lines, consistent with TCF results. Also, note that similar to the blurry ring function in Section III-A1a, pixels at the inner side of the $p_{\text{quad}}(\mathbf{x})$ have higher curvature compared to those on the outer side of the function.

c) *Image of Two Sine Waves*: We present the difference in curvature values for two sine functions with different frequencies. We place equally spaced isotropic Gaussian kernels on $y = \sin(f\mathbf{x})$ function. The sine function is defined as:

$$p_{\text{sine},f}(\mathbf{x}) = \sum_{j=1}^n K_I(\mathbf{x} - \mathbf{x}_{j,f}), \quad (20)$$

where $\mathbf{x}_{j,f} \in \{\mathbf{x} = [m, \sin(fm)]^T \mid m \in \mathcal{G}(50, -\pi, \pi)\}$. f is the frequency of the sine wave. We created an image using a higher-frequency sine function $p_{\text{sin,hf}}(\mathbf{x})$ with $f = 1.5$ and a lower-frequency sine function $p_{\text{sin,lf}}(\mathbf{x})$ with $f = 1.0$.

In the third column of Fig. 2, $p_{\text{sin,hf}}(\mathbf{x})$ and $p_{\text{sin,lf}}(\mathbf{x})$ are presented with their curvature results. With the proposed method, the curvature values at the local minima and local maxima in $p_{\text{sin,hf}}(\mathbf{x})$ are higher than those in $p_{\text{sin,lf}}(\mathbf{x})$.

d) *Image of A Sine Wave with Changing Amplitude and Frequency*: We show the change of the curvature values along a single sine function by modifying its amplitude and frequency. Equally spaced isotropic Gaussian kernels are placed on the $y = A \sin(fx)$ function, defined as:

$$p_{\text{sin},A,f}(\mathbf{x}) = \sum_{j=1}^n K_I(\mathbf{x} - \mathbf{x}_{j,A,f}), \quad (21)$$

where $\mathbf{x}_{j,A,f} \in \{\mathbf{x} = [m, A \sin(fm)]^T \mid m \in \mathcal{G}(50, -2\pi, 2\pi)\}$. f is the frequency and A is the amplitude of the sine wave. We generated an image by varying the values of A and f along the function. Specifically, for the first 25 samples (between the interval $[-2\pi, 0]$), we set $A = 1$ and $f = 2$, and for the remaining samples (between the interval $[0, 2\pi]$), we used $A = 3$ and $f = 1$.

The last column of Fig. 2 presents $p_{\text{sin},A,f}(\mathbf{x})$ with its curvature results. Along the function, the amplitude of the sine wave increases while the frequency decreases. TCF gives higher values at the local minima and maxima in $p_{\text{sin},A,f}(\mathbf{x})$ at the first half of the function since the frequency in the first half is higher than the second half. Also, the amplitude of the sine wave increases along the function, and this creates flat function parts where the curvature values are almost zero.

2) *Real Images*: In this part, we focus on four different two-dimensional real examples where we calculate the curvature of images from the MNIST [31], Retina [32], X-ray coronary angiogram [33] and River [34] image datasets. Fig. 3 provides four different two-dimensional real examples from the MNIST, Retina, Angiography, and River datasets respectively on the first row. Their curvature images calculated using TCF are presented in the second row. The intensity values on the curvature images represent the curvature values, with brighter pixels corresponding to higher values. Additionally, contrast enhancement is applied to the curvature values for visualization purposes. Gaussian kernels, as explained in (17), are applied to all the two-dimensional real examples using the scale matrix $\mathbf{S}_j = 0.5 \times \mathbf{I}_2$, where \mathbf{I}_2 is the two-dimensional identity matrix, and $k = 440$.

a) *MNIST Images*: We present sample images from the MNIST dataset with their curvature images in the first column of Fig. 3. The curvature of flat digit parts has lower values than other parts of the image. For example, curvature values for the flat part of digit 9 are lower than for curvature values of its non-flat parts. As in Section III-A1a, the curvature values are higher for pixels closer to the center of the digit 0, and these values decrease as the pixels move further away from the center.

b) *Retina Images*: We present a sample vessel segmentation image of the retina and its curvature results in the second column of Fig. 3. The segmented retina image contains branching points, tortuous vessel segments, and flat vessel segments. The branching points of vessel segments are where a vessel splits into multiple vessels or points where multiple vessel segments overlap.

The branching points are naturally high curvature regions because the vessels create a cross-shaped structure at the branching points. We observe this in TCF. Since the retinal

blood vessels start around the optic disc, there are many branching points around the optic disc where we observe high curvature values. The vessel segments at the left of the image have high tortuosity, whereas the segments on the right are almost flat. The curvature image has higher values for a tortuous vessel segment compared to other vessel segments in TCF. These results show that our method captures the tortuosity of the retinal blood vessels.

c) *Coronary Angiography Images*: The third column of Fig. 3 provides the interpolation function of a sample segmented coronary angiography and its curvature values calculated using TCF. Similar to the retina example from Section III-A2b, we observe high curvature values at the branching points and in highly tortuous regions. The vessel segment at the bottom left of the image is almost flat; on the other hand, the segment on the right is highly tortuous. TCF captures this difference in tortuosity and assigns low curvature values to the pixels in the flat vessel segment and high values to pixels in the tortuous regions.

d) *River Images*: The last row of Fig. 3 presents the interpolation function of a sample river segmentation image in the top row and its curvature values in the bottom row. In this application, a river bend (a meander) is one of the rivers' fundamental features. In TCF result, it is observed that the meanders of the river have high curvature values.

B. Three-Dimensional Results

This subsection includes results with three-dimensional artificial images with different curved structures and a real-world medical example.

1) *Artificial Images*: In this section, four different three-dimensional artificial images are presented: a blurry ring, a quadratic function, a sine wave, and a "V" shape. Fig. 4 displays these images in the first row, and their corresponding curvature images calculated using TCF are shown in the second row. The curvature results are presented using the Viridis colormap in the third row. Note that the curvature values are normalized within each image to have the same colormap for all images.

To generate these, we employ Gaussian kernels as described in (16), with the scale matrix $\mathbf{S}_j = \mathbf{I}_3$, where \mathbf{I}_3 represents the three-dimensional identity matrix, and $w_j = 1$ for $j \in \{1, \dots, n\}$. In each case, functions are defined by positioning evenly spaced isotropic Gaussian kernels, followed by the creation of images using uniform grids as explained in Sec. III-A1.

a) *Image of a Three-Dimensional Blurry Ring*: The three-dimensional blurry ring function is defined by placing equally spaced isotropic Gaussian kernels as in (22).

$$p_{\text{ring}_{3d}}(\mathbf{x}) = \sum_{j=1}^n K_I(\mathbf{x} - \mathbf{x}_j), \quad (22)$$

where $\mathbf{x}_j \in \{\mathbf{x} = [r \sin(\theta), r \cos(\theta), \sin(r)]^T \mid \theta \in \mathcal{G}(40, 0, 2\pi)\}$, and r is 2.

The first column in Fig. 4 presents $p_{\text{ring}_{3d}}(\mathbf{x})$ on the top row and its curvature results on the bottom. Similar to Section III-A1a, the curvature is reciprocal to the radius of the ring

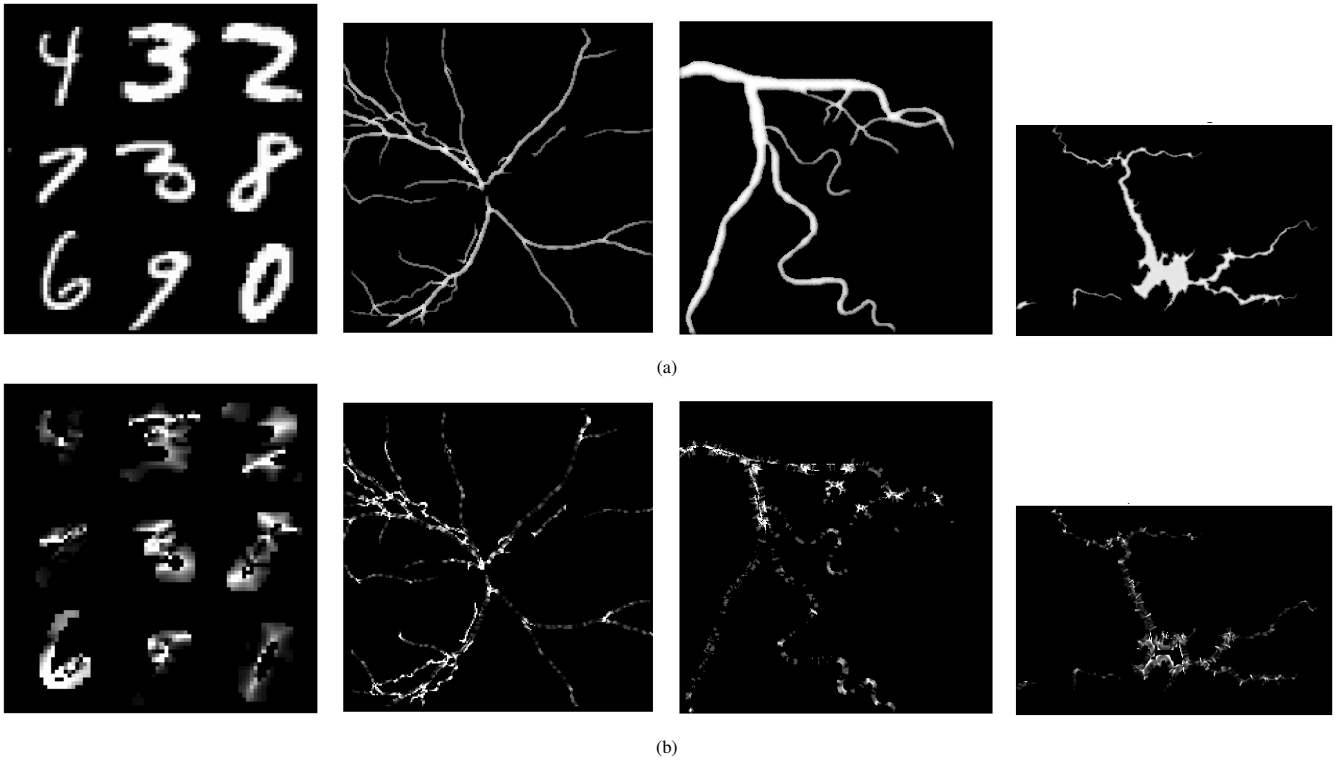


Fig. 3: (a) Two-dimensional interpolated images from the MNIST, Retina, Angiography, and River datasets are shown. (b) The curvature values of the two-dimensional images are calculated using TCF. Contrast enhancement is applied to the curvature values for visualization purposes. The intensity values represent the curvature values. Brighter pixels on the curvature plots correspond to higher values.

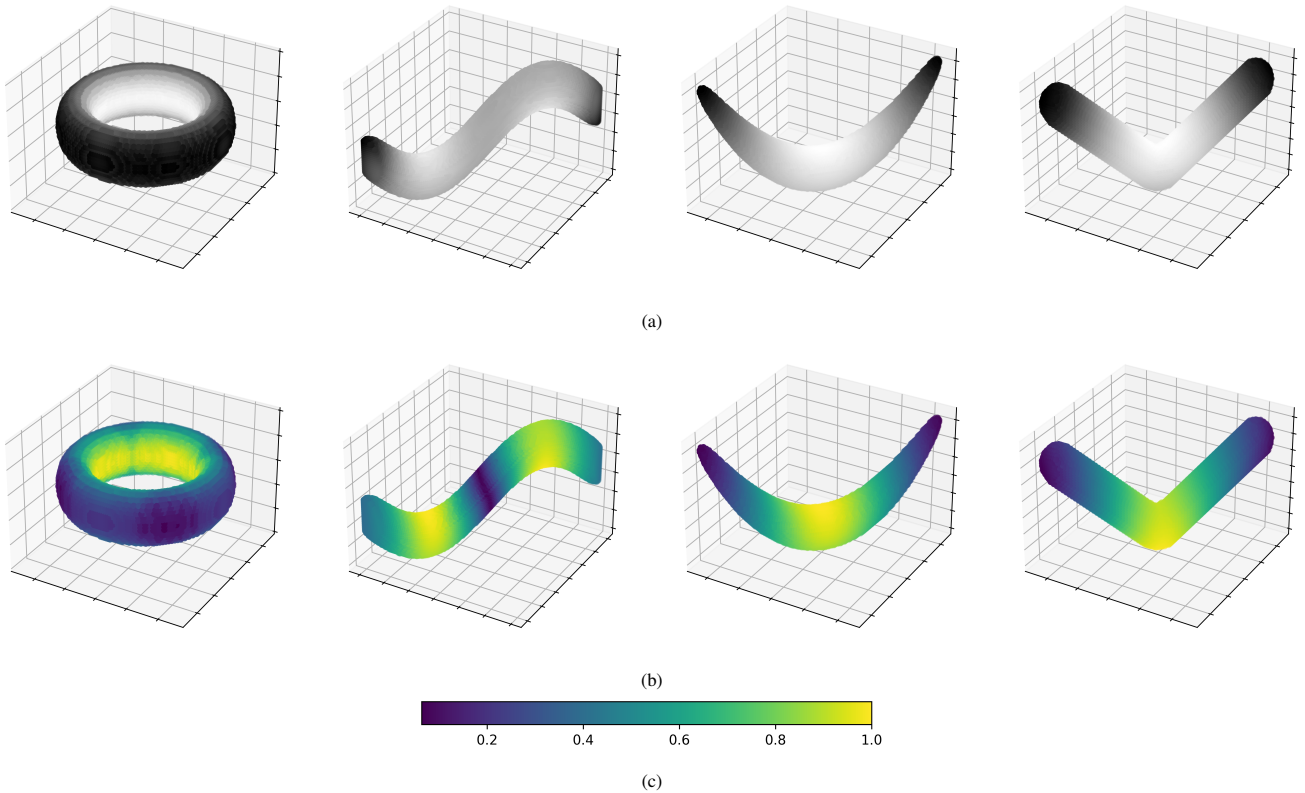


Fig. 4: (a) The first row includes the three-dimensional images of blurry-ring function $p_{\text{ring}_{3d}}(\mathbf{x})$, sine function $p_{\text{sin}_{3d}}(\mathbf{x})$, quadratic function $p_{\text{quad}_{3d}}(\mathbf{x})$ and "V" shaped function $p_{\text{abs}_{3d}}(\mathbf{x})$ function, respectively. (b) Their TCF results are presented in the second row. (c) Viridis colormap, displayed in the third row, is used for curvature plots.

at every point in the three-dimensional blurry ring function. Similarly, TCF gives higher values to the points closer to the center of the ring.

b) *Image of a Three-Dimensional Quadratic Function:* We established the quadratic function $p_{\text{quad}}(\mathbf{x})$ in three-dimension with isotropic Gaussian kernels as in (23).

$$p_{\text{quad_3d}}(\mathbf{x}) = \sum_{j=1}^n K_I(\mathbf{x} - \mathbf{x}_j), \quad (23)$$

where $\mathbf{x}_j \in \{\mathbf{x} = [m, m, m^2]^T \mid m \in \mathcal{G}(30, -1.25, 1.25)\}$.

The second column of Fig. 4 shows the image of the quadratic function $p_{\text{quad_3d}}(\mathbf{x})$ and its curvature results. Similar to the three-dimensional blurry ring function from Section III-B1a, pixels at the inner side of the function have higher curvature values than the points at the outer side. Also, as the pixels get further away from the global minimum, curvature values get lower.

c) *Image of a Three-Dimensional Sine Wave:* We define a sine function and place equally spaced isotropic Gaussian kernels as in (24).

$$p_{\text{sine_3d}}(\mathbf{x}) = \sum_{j=1}^n K_I(\mathbf{x} - \mathbf{x}_j), \quad (24)$$

where $\mathbf{x}_j \in \{\mathbf{x} = [m, m, \sin(m)]^T \mid m \in \mathcal{G}(40, -\pi, \pi)\}$.

Three-dimensional sine function $p_{\text{sine_3d}}(\mathbf{x})$ and its curvature result is given on the third row of Fig. 4. Pixels at the inner side of the curves have higher curvature values than the outer pixels. Moreover, the pixels closer to the maximum and minimum of the function have higher curvature values than the ones that are further away.

d) *Image of a Three-Dimensional "V" Shape:* A "V" shape function is defined and equally spaced isotropic Gaussian kernels are placed on it as in (25).

$$p_{\text{v-shape_3d}}(\mathbf{x}) = \sum_{j=1}^n K_I(\mathbf{x} - \mathbf{x}_j), \quad (25)$$

where $\mathbf{x}_j \in \{\mathbf{x} = [m, m, |m|]^T \mid m \in \mathcal{G}(20, -1.0, 1.0)\}$.

The last column of Fig. 4 shows the image of the "V" shape function $p_{\text{v-shape_3d}}(\mathbf{x})$ on the top row and its TCF results on the bottom. Like the three-dimensional quadratic function from Section III-B1b, as the pixels get closer to the global minimum, curvature values get higher.

2) *Real Images:* This part focuses on a three-dimensional real example from the Computed Tomography Angiography dataset [35].

We calculated the curvature of a segmented coronary artery image from a three-dimensional computed tomography angiography (CTA). We employed Gaussian kernels as the interpolation method, as defined in (17), where in three dimensions, $\tilde{\mathbf{x}}_j \in \mathbb{Z}^3$, and $K_{S_j}(\cdot) : \mathbb{R}^3 \rightarrow \mathbb{R}$ is the interpolation kernel. In this example, we used a scale matrix $\mathbf{S}_j = \mathbf{I}_3$, where \mathbf{I}_3 is the three-dimensional identity matrix, and set $k = 20$.

Fig. 5 presents the interpolated image in the first row and the curvature results in the second row, with XZ and YZ plane views shown in the second, third, and fourth columns. Contrast enhancement is added using histogram equalization

[36] to the curvature results to make high curvature values more visible. Viridis colormap, presented in the third row, is used for curvature results. Similar to Section III-A2c, high curvature values at the branching points and twisted vessels are observed in this example, as expected.

IV. CONCLUSION

This paper defines local tubular curvature and presents a methodology to calculate local curvature of tubular objects using interpolated intensity images. The proposed filter approach implicitly calculates the tubular curvature locally for a bundle of parallel curves that extend along the tube. The method does not require the extraction of centerlines or curves from the image. To our knowledge, the presented TCF methodology is the first of its kind, in the sense that it focuses on local curvature calculations for curves that traverse space along the tubular object, and achieves implicit calculations by determining the acceleration vectors for these curves using the eigenvectors of Hessian matrices of the intensity function. TCF exhibits sensitivity to varying curvature levels in a tube along the cross-section. Specifically, results on synthetic and real images demonstrate that this method can highlight tortuous regions in vessels and also detect curvature differences between points on the inner and outer sides of curved structures, unlike centerline-based methods.

One domain where TCF can be particularly useful is medical domains that require vasculature curvature analyses from images. Biological vascular structures are often non-uniform in diameter, and may exhibit various conformations in both normal physiology and disease states. Measuring the curvature of anatomic structures is a common task performed by clinicians and increasingly performed by automated techniques. In some diseases, as in the case of retinopathy of prematurity (ROP), a leading cause of childhood blindness, the dilation and tortuosity of retinal vessel network is a key component of disease classification; in general, the more dilated and tortuous the vessels, the more severe the ROP. This has led the quantification of "vascular severity" to become a key biomarker target for image analysis techniques. One future application of this technique would be to apply the TCF methodology to better understand the relationship between local retinal vessel tortuosity and incident disease progression. The TCF technique has an advantage over deep learning techniques in the sense that it is interpretable, and because it can be applied both locally and globally within medical images, and across image types in a way that many convolutional neural networks may have generalizability challenges.

APPENDIX A

DERIVATION OF DEFINITION 1

Given a point $\mathbf{x} \in \mathbb{R}^2$, let $f(\mathbf{x})$ be the logarithm of the interpolation function $p(\mathbf{x})$. Let us define $p(\mathbf{x})$ and $f(\mathbf{x})$ as:

$$p(\mathbf{x}) = \sum_{j=1}^n w_j K_{S_j}(\mathbf{x} - \mathbf{x}_j), \quad (26)$$

$$f(\mathbf{x}) = \log(p(\mathbf{x})), \quad (27)$$

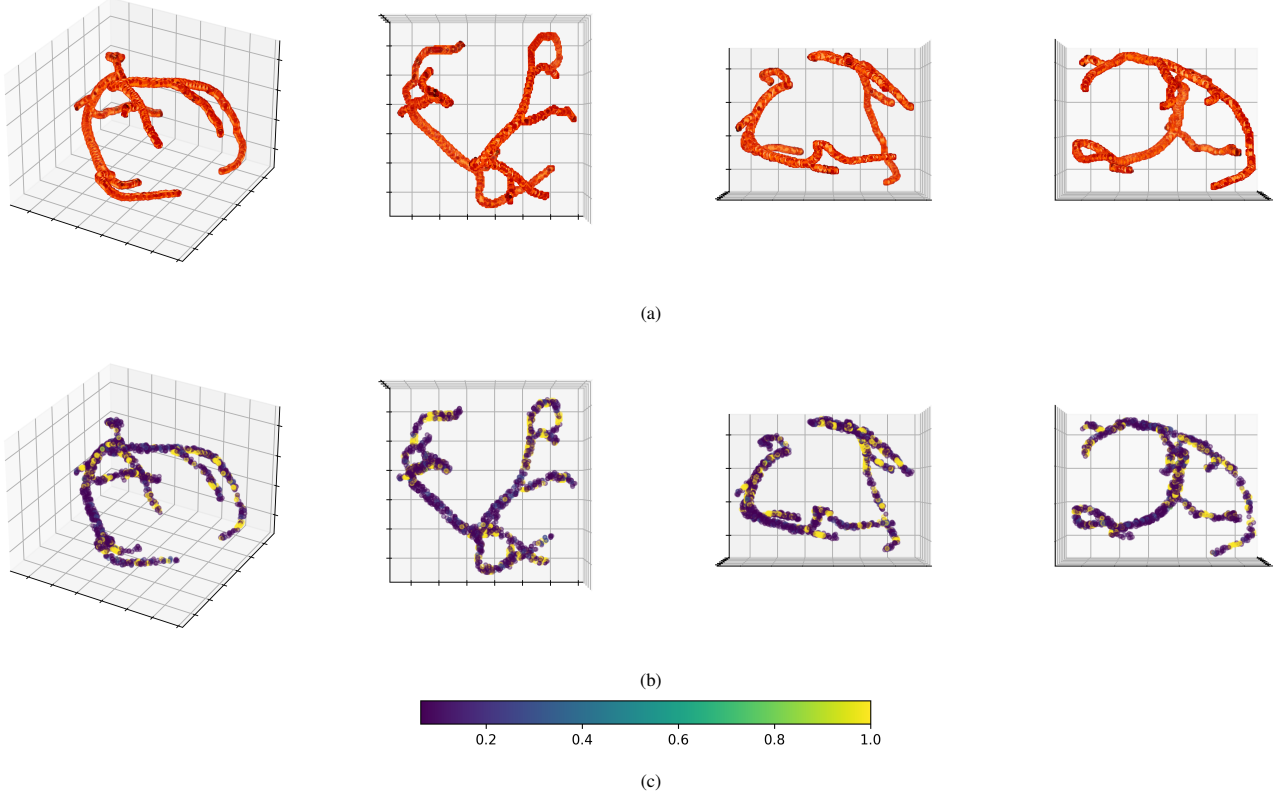


Fig. 5: (a) The first row presents the three-dimensional coronary angiography with views from different planes (XY, XZ, YZ, respectively). (b) The second row displays their TCF results. For visualization purposes, the contrast of the curvature results is enhanced using histogram equalization, as described in [36]. (c) Viridis colormap, presented in the third row, is used for curvature plots.

where $K_{S_j}(\cdot) : \mathbb{R}^2 \rightarrow \mathbb{R}$ is the interpolation kernel with scale matrix S_j , \mathbf{x} and $w_j \in \mathbb{R}_+$, $j \in \{1, \dots, n\}$, represent the location and intensity of a point indexed by $j \in \{1, \dots, n\}$, respectively. n is the number of points. Note that $f(\mathbf{x})$ can be defined as any other monotonically increasing function of the interpolation function $p(\mathbf{x})$. In Ozertem et al. [29], it is demonstrated that the principal surfaces, represented as a set of points, remain invariant when subjected to monotonic transformations of the pdf. By selecting the logarithm as the monotonically increasing function, the authors illustrate that the local Hessian eigendirections evolve into linear paths. Additionally, if the density becomes Gaussian, principal surface projections of points coincide with those one would obtain via linear PCA. In the context of this paper, the exponential-quadratic nature of Gaussian kernel based interpolation makes natural-logarithm a suitable choice.

Let $\mathbf{g}(\mathbf{x})$ be the transpose of the gradient of $f(\mathbf{x})$, $\mathbf{g}_p(\mathbf{x})$ be the transpose of the gradient of $p(\mathbf{x})$ and $\mathbf{H}(\mathbf{x})$ be the Hessian of $f(\mathbf{x})$. For simplicity, we drop (\mathbf{x}) notation from the functions for the rest of the paper. We define \mathbf{g} and \mathbf{H} as:

$$\mathbf{g} = \nabla^T f = \frac{\nabla^T p}{p} = \frac{\mathbf{g}_p}{p}, \quad (28)$$

$$\begin{aligned} \mathbf{H} &= \nabla \mathbf{g} = \frac{\nabla^T \nabla p}{p} - \frac{\nabla \nabla^T p}{p^2} \\ &= \frac{\nabla \mathbf{g}_p}{p} - \mathbf{g} \mathbf{g}^T. \end{aligned} \quad (29)$$

We will need $\frac{\partial \mathbf{H}}{\partial x_i}$ later for (6) where x_i is the i -th dimension of \mathbf{x} .

$$\begin{aligned} \frac{\partial \mathbf{H}}{\partial x_i} &= \frac{\frac{\partial \nabla^T \nabla p}{\partial x_i} p - \nabla^T \nabla p \frac{\partial p}{\partial x_i}}{p^2} \\ &\quad - \frac{(\frac{\partial \nabla p}{\partial x_i} \nabla^T p + \nabla p \frac{\partial \nabla^T p}{\partial x_i}) p^2}{p^4} + \frac{2p \nabla \nabla^T p \frac{\partial p}{\partial x_i}}{p^4} \\ &= \frac{1}{p} \frac{\partial \nabla^T \nabla p}{\partial x_i} - \frac{1}{p^2} (\nabla^T \nabla p \frac{\partial p}{\partial x_i} + \frac{\partial \nabla p}{\partial x_i} \nabla^T p \\ &\quad + \nabla p \frac{\partial \nabla^T p}{\partial x_i}) + \frac{2}{p^3} \nabla p \nabla^T p \frac{\partial p}{\partial x_i}. \end{aligned} \quad (30)$$

Following the steps from (5)-(15), Hessian and its derivatives are defined to calculate the acceleration vector point \mathbf{x} , where $\{(\lambda_1(\mathbf{x}), \mathbf{q}_1(\mathbf{x})), (\lambda_2(\mathbf{x}), \mathbf{q}_2(\mathbf{x}))\}$ are the eigenvalue-eigenvector pairs of $\mathbf{H}(\mathbf{x})$, and $|\lambda_1(\mathbf{x})| > |\lambda_2(\mathbf{x})|$. We define \mathbf{q}_i as follows for two-dimensional inputs:

$$\mathbf{q}_i = [\mathbf{q}_{i1} \quad \mathbf{q}_{i2}]^T. \quad (31)$$

$\mathbf{H}(\mathbf{x})$ is decomposed into its eigenvectors in (4), where \mathbf{Q} is the 2×2 matrix whose i th column is the eigenvector \mathbf{q}_i , and $\mathbf{\Lambda}$ is the diagonal matrix whose diagonal elements are the corresponding eigenvalues.

Therefore, $\mathbf{H}(\mathbf{x})$ for two-dimensional inputs are defined as:

$$\mathbf{H}(\mathbf{x}) = \begin{bmatrix} \mathbf{q}_1 \\ \mathbf{q}_2 \end{bmatrix}^T \begin{bmatrix} \lambda_1 & 0 \\ 0 & \lambda_2 \end{bmatrix} \begin{bmatrix} \mathbf{q}_1 \\ \mathbf{q}_2 \end{bmatrix}. \quad (32)$$

We calculate $\partial \mathbf{q}_1(\mathbf{x})/\partial \mathbf{x}$ by taking derivatives of eigen decomposition of Hessian in (32). We define $\mathbf{T}_i(\mathbf{x})$, $\mathbf{V}_i(\mathbf{x})$ and $\mathbf{L}_i(\mathbf{x})$ in (6)-(8), respectively.

\mathbf{T}_i for $i = 1$ is derived in (33).

$$\begin{aligned} \mathbf{T}_1 = & \lambda_1 \frac{\partial \mathbf{q}_1}{\partial x_1} \mathbf{q}_1^T + \lambda_2 \frac{\partial \mathbf{q}_2}{\partial x_1} \mathbf{q}_2^T + l_{11} \mathbf{q}_1 \mathbf{q}_1^T \\ & + l_{12} \mathbf{q}_2 \mathbf{q}_2^T + \lambda_1 \mathbf{q}_1 \frac{\partial \mathbf{q}_1}{\partial x_1}^T + \lambda_2 \mathbf{q}_2 \frac{\partial \mathbf{q}_2}{\partial x_1}^T. \end{aligned} \quad (33)$$

Linear equations for $i = 1$ from (13) are derived in (34)-(39). From (33), we have three linear equations which are defined in (34)-(36) for $i = 1$.

$$\begin{aligned} t_{111} = & \lambda_1 v_{111} q_{11} + \lambda_2 v_{112} q_{21} + l_{11} q_{11} q_{11} \\ & + l_{12} q_{21} q_{21} + \lambda_1 q_{11} v_{111} + \lambda_2 q_{21} v_{112}, \end{aligned} \quad (34)$$

$$\begin{aligned} t_{112} = & \lambda_1 v_{111} q_{12} + \lambda_2 v_{112} q_{22} + l_{11} q_{11} q_{12} \\ & + l_{12} q_{21} q_{22} + \lambda_1 q_{11} v_{121} + \lambda_2 q_{21} v_{122}, \end{aligned} \quad (35)$$

$$\begin{aligned} t_{122} = & \lambda_1 v_{121} q_{12} + \lambda_2 v_{122} q_{22} + l_{11} q_{12} q_{12} \\ & + l_{12} q_{22} q_{22} + \lambda_1 q_{12} v_{121} + \lambda_2 q_{22} v_{122}. \end{aligned} \quad (36)$$

Two properties of eigenvectors are: 1) Eigenvectors are unit vectors, 2) Eigenvectors are perpendicular to each other. Following these properties, we derived three linear equations in (37)-(39) where (37)-(38) are derived from the first property of eigenvectors and (39) is from the second.

$$0 = q_{11} v_{111} + q_{12} v_{121}, \quad (37)$$

$$0 = q_{21} v_{112} + q_{22} v_{122}, \quad (38)$$

$$0 = q_{21} v_{111} + q_{22} v_{121} + q_{11} v_{112} + q_{12} v_{122}. \quad (39)$$

We have 6 equations and 12 unknowns for two-dimensional input. Writing the set of linear equations, we obtain (13) and (15). Then, the elements of $\mathbf{V}(\mathbf{x})$ and $\mathbf{L}(\mathbf{x})$ are found using a linear solver so that $\partial \mathbf{q}_1(\mathbf{x})/\partial \mathbf{x}$ are calculated from $\mathbf{V}(\mathbf{x})$ to obtain the acceleration vector at point \mathbf{x} .

APPENDIX B

GENERALIZATION OF CURVATURE FILTERS TO FUNCTIONS OF N-DIMENSIONAL INPUT

Similar to two-dimensional functions, we calculate the curvature of an N-dimensional function. Let $\mathbf{x} \in \mathbb{R}^N$ represent a point in the function $f(\mathbf{x}) : \mathbb{R}^N \rightarrow \mathbb{R}$ and w_j , \mathbf{x}_j are the intensity and location of a point indexed by $j \in \{1, \dots, n\}$, respectively. n is the number of points. We define an interpolation function $p(\mathbf{x})$ as:

$$p(\mathbf{x}) = \sum_{j=1}^n w_j K_{S_j}(\mathbf{x} - \mathbf{x}_j), \quad (40)$$

where $K_{S_j}(\cdot) : \mathbb{R}^N \rightarrow \mathbb{R}$ is the interpolation kernel with scale matrix \mathbf{S}_j . At any point \mathbf{x} on the function $f(\mathbf{x})$, \mathbf{q}_1 is the unit velocity vector of the curve s , which is the curve that is parallel to the principle curve of the function. With this definition of the unit velocity vector, the change in the direction of the velocity vector is due to the curvature of the function. Following the definition of acceleration vector in **Definition 1**, we need to find the direction derivatives of

\mathbf{q}_1 , i.e., $[\partial \mathbf{q}_1/\partial x_1 \cdots \partial \mathbf{q}_1/\partial x_N]$. Following the same steps from (5)-(12), Hessian and its derivatives are defined for the n-dimensional function.

A. Three-Dimensional Input

For three-dimensional inputs, following the steps from (5)-(15), Hessian and its derivatives are defined to calculate the acceleration vector point of $\mathbf{x} \in \mathbb{R}^3$ where $\{(\lambda_1(\mathbf{x}), \mathbf{q}_1(\mathbf{x})), (\lambda_2(\mathbf{x}), \mathbf{q}_2(\mathbf{x})), (\lambda_3(\mathbf{x}), \mathbf{q}_3(\mathbf{x}))\}$ are the eigenvalue-eigenvector pairs of $\mathbf{H}(\mathbf{x})$, and $|\lambda_1(\mathbf{x})| > |\lambda_2(\mathbf{x})| > |\lambda_3(\mathbf{x})|$. We define \mathbf{q}_i as follows for three-dimensional inputs:

$$\mathbf{q}_i = [q_{i1} \quad q_{i2} \quad q_{i3}]^T. \quad (41)$$

$\mathbf{H}(\mathbf{x})$ is decomposed into its eigenvectors in (4), where \mathbf{Q} is the 3×3 matrix whose i th column is the eigenvector \mathbf{q}_i , and $\mathbf{\Lambda}$ is the diagonal matrix whose diagonal elements are the corresponding eigenvalues. Therefore, $\mathbf{H}(\mathbf{x})$ for three-dimensional functions are defined as:

$$\mathbf{H}(\mathbf{x}) = \begin{bmatrix} \mathbf{q}_1 \\ \mathbf{q}_2 \\ \mathbf{q}_3 \end{bmatrix}^T \begin{bmatrix} \lambda_1 & 0 & 0 \\ 0 & \lambda_2 & 0 \\ 0 & 0 & \lambda_3 \end{bmatrix} \begin{bmatrix} \mathbf{q}_1 \\ \mathbf{q}_2 \\ \mathbf{q}_3 \end{bmatrix}, \quad (42)$$

We calculate $\partial \mathbf{q}_1(\mathbf{x})/\partial \mathbf{x}$ by taking derivatives of eigen decomposition of Hessian in (42). We define $\mathbf{T}_i(\mathbf{x})$, $\mathbf{V}_i(\mathbf{x})$ and $\mathbf{L}_i(\mathbf{x})$ respectively:

$$\mathbf{T}_i(\mathbf{x}) = \frac{\partial \mathbf{H}(\mathbf{x})}{\partial x_i} = \begin{bmatrix} t_{i11} & t_{i12} & t_{i13} \\ t_{i21} & t_{i22} & t_{i23} \\ t_{i31} & t_{i32} & t_{i33} \end{bmatrix}, \quad (43)$$

$$\mathbf{V}_i(\mathbf{x}) = \frac{\partial \mathbf{Q}(\mathbf{x})}{\partial x_i} = \begin{bmatrix} \frac{\partial \mathbf{q}_1}{\partial x_i} \\ \frac{\partial \mathbf{q}_2}{\partial x_i} \\ \frac{\partial \mathbf{q}_3}{\partial x_i} \end{bmatrix}^T = \begin{bmatrix} v_{i11} & v_{i12} & v_{i13} \\ v_{i21} & v_{i22} & v_{i23} \\ v_{i31} & v_{i32} & v_{i33} \end{bmatrix}, \quad (44)$$

$$\mathbf{L}_i(\mathbf{x}) = \begin{bmatrix} \frac{\partial \lambda_1}{\partial x_i} & 0 & 0 \\ 0 & \frac{\partial \lambda_2}{\partial x_i} & 0 \\ 0 & 0 & \frac{\partial \lambda_3}{\partial x_i} \end{bmatrix} = \begin{bmatrix} l_{i1} & 0 & 0 \\ 0 & l_{i2} & 0 \\ 0 & 0 & l_{i3} \end{bmatrix}. \quad (45)$$

We defined \mathbf{T}_i in (43) and we know that \mathbf{T}_i is symmetric. We can derive \mathbf{T}_i for $i = 1$ in (46).

$$\begin{aligned} \mathbf{T}_1 = & \lambda_1 \frac{\partial \mathbf{q}_1}{\partial x_1} \mathbf{q}_1^T + \lambda_2 \frac{\partial \mathbf{q}_2}{\partial x_1} \mathbf{q}_2^T + \lambda_3 \frac{\partial \mathbf{q}_3}{\partial x_1} \mathbf{q}_3^T \\ & + l_{11} \mathbf{q}_1 \mathbf{q}_1^T + l_{12} \mathbf{q}_2 \mathbf{q}_2^T + l_{13} \mathbf{q}_3 \mathbf{q}_3^T \\ & + \lambda_1 \mathbf{q}_1 \frac{\partial \mathbf{q}_1}{\partial x_1}^T + \lambda_2 \mathbf{q}_2 \frac{\partial \mathbf{q}_2}{\partial x_1}^T + \lambda_3 \mathbf{q}_3 \frac{\partial \mathbf{q}_3}{\partial x_1}^T. \end{aligned} \quad (46)$$

Also, using the two properties of eigenvectors, we have the following set of additional equations:

$$\frac{\partial \|\mathbf{q}_1(\mathbf{x})\|^2}{\partial x_i} = 2 \mathbf{q}_1^T \frac{\partial \mathbf{q}_1}{\partial x_i} = 0, \quad (47)$$

$$\frac{\partial \|\mathbf{q}_2(\mathbf{x})\|^2}{\partial x_i} = 2 \mathbf{q}_2^T \frac{\partial \mathbf{q}_2}{\partial x_i} = 0, \quad (48)$$

$$\frac{\partial \|\mathbf{q}_3(\mathbf{x})\|^2}{\partial x_i} = 2 \mathbf{q}_3^T \frac{\partial \mathbf{q}_3}{\partial x_i} = 0, \quad (49)$$

$$\frac{\partial \mathbf{q}_1^T \mathbf{q}_2}{\partial x_i} = \mathbf{q}_1^T \frac{\partial \mathbf{q}_2}{\partial x_i} + \frac{\partial \mathbf{q}_1^T}{\partial x_i} \mathbf{q}_2 = 0, \quad (50)$$

$$\frac{\partial \mathbf{q}_1^T \mathbf{q}_3}{\partial x_i} = \mathbf{q}_1^T \frac{\partial \mathbf{q}_3}{\partial x_i} + \frac{\partial \mathbf{q}_1^T}{\partial x_i} \mathbf{q}_3 = 0, \quad (51)$$

$$\frac{\partial \mathbf{q}_2^T \mathbf{q}_3}{\partial x_i} = \mathbf{q}_2^T \frac{\partial \mathbf{q}_3}{\partial x_i} + \frac{\partial \mathbf{q}_2^T}{\partial x_i} \mathbf{q}_3 = 0. \quad (52)$$

Linear equations of three-dimensional input for $i = 1$ are derived as in (53)-(64). From (46), we derived six linear equations which are defined in (53)-(58) for $i = 1$.

$$\begin{aligned} \mathbf{t}_{111} = & \lambda_1 \mathbf{v}_{111} \mathbf{q}_{11} + \lambda_2 \mathbf{v}_{112} \mathbf{q}_{21} + \lambda_3 \mathbf{v}_{113} \mathbf{q}_{31} \\ & + l_{11} \mathbf{q}_{11} \mathbf{q}_{11} + l_{12} \mathbf{q}_{21} \mathbf{q}_{21} + l_{13} \mathbf{q}_{31} \mathbf{q}_{31} \\ & + \lambda_1 \mathbf{q}_{11} \mathbf{v}_{111} + \lambda_2 \mathbf{q}_{21} \mathbf{v}_{112} + \lambda_3 \mathbf{q}_{31} \mathbf{v}_{113}, \end{aligned} \quad (53)$$

$$\begin{aligned} \mathbf{t}_{112} = & \lambda_1 \mathbf{v}_{111} \mathbf{q}_{12} + \lambda_2 \mathbf{v}_{112} \mathbf{q}_{22} + \lambda_3 \mathbf{v}_{113} \mathbf{q}_{32} \\ & + l_{11} \mathbf{q}_{11} \mathbf{q}_{12} + l_{12} \mathbf{q}_{21} \mathbf{q}_{22} + l_{13} \mathbf{q}_{31} \mathbf{q}_{32} \\ & + \lambda_1 \mathbf{q}_{11} \mathbf{v}_{121} + \lambda_2 \mathbf{q}_{21} \mathbf{v}_{122} + \lambda_3 \mathbf{q}_{31} \mathbf{v}_{123}, \end{aligned} \quad (54)$$

$$\begin{aligned} \mathbf{t}_{113} = & \lambda_1 \mathbf{v}_{111} \mathbf{q}_{13} + \lambda_2 \mathbf{v}_{112} \mathbf{q}_{23} + \lambda_3 \mathbf{v}_{113} \mathbf{q}_{33} \\ & + l_{11} \mathbf{q}_{11} \mathbf{q}_{13} + l_{12} \mathbf{q}_{21} \mathbf{q}_{23} + l_{13} \mathbf{q}_{31} \mathbf{q}_{33} \\ & + \lambda_1 \mathbf{q}_{11} \mathbf{v}_{131} + \lambda_2 \mathbf{q}_{21} \mathbf{v}_{132} + \lambda_3 \mathbf{q}_{31} \mathbf{v}_{133}, \end{aligned} \quad (55)$$

$$\begin{aligned} \mathbf{t}_{122} = & \lambda_1 \mathbf{v}_{121} \mathbf{q}_{12} + \lambda_2 \mathbf{v}_{122} \mathbf{q}_{22} + \lambda_3 \mathbf{v}_{123} \mathbf{q}_{32} \\ & + l_{11} \mathbf{q}_{12} \mathbf{q}_{12} + l_{12} \mathbf{q}_{22} \mathbf{q}_{22} + l_{13} \mathbf{q}_{32} \mathbf{q}_{32} \\ & + \lambda_1 \mathbf{q}_{12} \mathbf{v}_{121} + \lambda_2 \mathbf{q}_{22} \mathbf{v}_{122} + \lambda_3 \mathbf{q}_{32} \mathbf{v}_{123}, \end{aligned} \quad (56)$$

$$\begin{aligned} \mathbf{t}_{123} = & \lambda_1 \mathbf{v}_{121} \mathbf{q}_{13} + \lambda_2 \mathbf{v}_{122} \mathbf{q}_{23} + \lambda_3 \mathbf{v}_{123} \mathbf{q}_{33} \\ & + l_{11} \mathbf{q}_{12} \mathbf{q}_{13} + l_{12} \mathbf{q}_{22} \mathbf{q}_{23} + l_{13} \mathbf{q}_{32} \mathbf{q}_{33} \\ & + \lambda_1 \mathbf{q}_{12} \mathbf{v}_{131} + \lambda_2 \mathbf{q}_{22} \mathbf{v}_{132} + \lambda_3 \mathbf{q}_{32} \mathbf{v}_{133}, \end{aligned} \quad (57)$$

$$\begin{aligned} \mathbf{t}_{133} = & \lambda_1 \mathbf{v}_{131} \mathbf{q}_{13} + \lambda_2 \mathbf{v}_{132} \mathbf{q}_{23} + \lambda_3 \mathbf{v}_{133} \mathbf{q}_{33} \\ & + l_{11} \mathbf{q}_{13} \mathbf{q}_{13} + l_{12} \mathbf{q}_{23} \mathbf{q}_{23} + l_{13} \mathbf{q}_{33} \mathbf{q}_{33} \\ & + \lambda_1 \mathbf{q}_{13} \mathbf{v}_{131} + \lambda_2 \mathbf{q}_{23} \mathbf{v}_{132} + \lambda_3 \mathbf{q}_{33} \mathbf{v}_{133}. \end{aligned} \quad (58)$$

Following the properties of eigenvectors in (47)-(52), six linear equations in (59)-(64) are derived.

$$0 = \mathbf{q}_{11} \mathbf{v}_{111} + \mathbf{q}_{12} \mathbf{v}_{121} + \mathbf{q}_{13} \mathbf{v}_{131}, \quad (59)$$

$$0 = \mathbf{q}_{21} \mathbf{v}_{112} + \mathbf{q}_{22} \mathbf{v}_{122} + \mathbf{q}_{23} \mathbf{v}_{132}, \quad (60)$$

$$0 = \mathbf{q}_{31} \mathbf{v}_{113} + \mathbf{q}_{32} \mathbf{v}_{123} + \mathbf{q}_{33} \mathbf{v}_{133}, \quad (61)$$

$$\begin{aligned} 0 = & \mathbf{q}_{21} \mathbf{v}_{111} + \mathbf{q}_{22} \mathbf{v}_{121} + \mathbf{q}_{23} \mathbf{v}_{131} \\ & + \mathbf{q}_{11} \mathbf{v}_{112} + \mathbf{q}_{12} \mathbf{v}_{122} + \mathbf{q}_{13} \mathbf{v}_{132}, \end{aligned} \quad (62)$$

$$\begin{aligned} 0 = & \mathbf{q}_{31} \mathbf{v}_{111} + \mathbf{q}_{32} \mathbf{v}_{121} + \mathbf{q}_{33} \mathbf{v}_{131} \\ & + \mathbf{q}_{11} \mathbf{v}_{113} + \mathbf{q}_{12} \mathbf{v}_{123} + \mathbf{q}_{13} \mathbf{v}_{133}, \end{aligned} \quad (63)$$

$$\begin{aligned} 0 = & \mathbf{q}_{21} \mathbf{v}_{113} + \mathbf{q}_{22} \mathbf{v}_{123} + \mathbf{q}_{23} \mathbf{v}_{133} \\ & + \mathbf{q}_{31} \mathbf{v}_{112} + \mathbf{q}_{32} \mathbf{v}_{122} + \mathbf{q}_{33} \mathbf{v}_{132}. \end{aligned} \quad (64)$$

Using the set of linear equations in (53)-(58), we obtain (65), where we define \mathbf{M} in (66). The elements of $\mathbf{V}(\mathbf{x})$ and $\mathbf{L}(\mathbf{x})$ are found by solving the system of linear equations to obtain $\partial \mathbf{q}_1(\mathbf{x})/\partial \mathbf{x}$ from $\mathbf{V}(\mathbf{x})$. The acceleration vector at point \mathbf{x} is calculated as in (1).

$$\begin{bmatrix} \mathbf{t}_{111} \\ \mathbf{t}_{112} \\ \mathbf{t}_{113} \\ \mathbf{t}_{122} \\ \mathbf{t}_{123} \\ \mathbf{t}_{133} \\ 0 \\ 0 \\ 0 \\ 0 \\ 0 \\ 0 \end{bmatrix} = \mathbf{M} \begin{bmatrix} \mathbf{v}_{111} \\ \mathbf{v}_{112} \\ \mathbf{v}_{113} \\ l_{11} \\ l_{12} \\ l_{13} \\ \mathbf{v}_{121} \\ \mathbf{v}_{122} \\ \mathbf{v}_{123} \\ \mathbf{v}_{131} \\ \mathbf{v}_{132} \\ \mathbf{v}_{133} \end{bmatrix}, \quad \begin{bmatrix} \mathbf{t}_{211} \\ \mathbf{t}_{212} \\ \mathbf{t}_{213} \\ \mathbf{t}_{222} \\ \mathbf{t}_{223} \\ \mathbf{t}_{233} \\ 0 \\ 0 \\ 0 \\ 0 \\ 0 \\ 0 \end{bmatrix} = \mathbf{M} \begin{bmatrix} \mathbf{v}_{211} \\ \mathbf{v}_{212} \\ \mathbf{v}_{213} \\ l_{21} \\ l_{22} \\ l_{23} \\ \mathbf{v}_{221} \\ \mathbf{v}_{222} \\ \mathbf{v}_{223} \\ \mathbf{v}_{231} \\ \mathbf{v}_{232} \\ \mathbf{v}_{233} \end{bmatrix} \quad \text{and} \quad \begin{bmatrix} \mathbf{t}_{311} \\ \mathbf{t}_{312} \\ \mathbf{t}_{313} \\ \mathbf{t}_{322} \\ \mathbf{t}_{323} \\ \mathbf{t}_{333} \\ 0 \\ 0 \\ 0 \\ 0 \\ 0 \\ 0 \end{bmatrix} = \mathbf{M} \begin{bmatrix} \mathbf{v}_{311} \\ \mathbf{v}_{312} \\ \mathbf{v}_{313} \\ l_{31} \\ l_{32} \\ l_{33} \\ \mathbf{v}_{321} \\ \mathbf{v}_{322} \\ \mathbf{v}_{323} \\ \mathbf{v}_{331} \\ \mathbf{v}_{332} \\ \mathbf{v}_{333} \end{bmatrix}, \quad (65)$$

$$\mathbf{n} \begin{bmatrix} 2\lambda_1 \mathbf{q}_{11} & 2\lambda_2 \mathbf{q}_{21} & 2\lambda_3 \mathbf{q}_{31} & \mathbf{q}_{11}^2 & \mathbf{q}_{21}^2 & \mathbf{q}_{31}^2 & 0 & 0 & 0 & 0 & 0 & 0 \\ \lambda_1 \mathbf{q}_{12} & \lambda_2 \mathbf{q}_{22} & \lambda_3 \mathbf{q}_{32} & \mathbf{q}_{11} \mathbf{q}_{12} & \mathbf{q}_{21} \mathbf{q}_{22} & \mathbf{q}_{31} \mathbf{q}_{32} & \lambda_1 \mathbf{q}_{11} & \lambda_2 \mathbf{q}_{21} & \lambda_3 \mathbf{q}_{31} & 0 & 0 & 0 \\ \lambda_1 \mathbf{q}_{13} & \lambda_2 \mathbf{q}_{23} & \lambda_3 \mathbf{q}_{33} & \mathbf{q}_{11} \mathbf{q}_{13} & \mathbf{q}_{21} \mathbf{q}_{23} & \mathbf{q}_{31} \mathbf{q}_{33} & 0 & 0 & 0 & \lambda_1 \mathbf{q}_{11} & \lambda_2 \mathbf{q}_{21} & \lambda_3 \mathbf{q}_{31} \\ 0 & 0 & 0 & \mathbf{q}_{12}^2 & \mathbf{q}_{22}^2 & \mathbf{q}_{32}^2 & 2\lambda_1 \mathbf{q}_{12} & 2\lambda_2 \mathbf{q}_{22} & 2\lambda_3 \mathbf{q}_{32} & 0 & 0 & 0 \\ 0 & 0 & 0 & \mathbf{q}_{12} \mathbf{q}_{13} & \mathbf{q}_{22} \mathbf{q}_{23} & \mathbf{q}_{32} \mathbf{q}_{33} & \lambda_1 \mathbf{q}_{13} & \lambda_2 \mathbf{q}_{23} & \lambda_3 \mathbf{q}_{33} & \lambda_1 \mathbf{q}_{12} & \lambda_2 \mathbf{q}_{22} & \lambda_3 \mathbf{q}_{32} \\ 0 & 0 & 0 & \mathbf{q}_{13}^2 & \mathbf{q}_{23}^2 & \mathbf{q}_{33}^2 & 0 & 0 & 0 & 2\lambda_1 \mathbf{q}_{13} & 2\lambda_2 \mathbf{q}_{23} & 2\lambda_3 \mathbf{q}_{33} \\ \mathbf{q}_{11} & 0 & 0 & 0 & 0 & 0 & \mathbf{q}_{12} & 0 & 0 & \mathbf{q}_{13} & 0 & 0 \\ 0 & \mathbf{q}_{21} & 0 & 0 & 0 & 0 & 0 & \mathbf{q}_{22} & 0 & 0 & \mathbf{q}_{23} & 0 \\ 0 & 0 & \mathbf{q}_{31} & 0 & 0 & 0 & 0 & 0 & \mathbf{q}_{32} & 0 & 0 & \mathbf{q}_{33} \\ \mathbf{q}_{21} & \mathbf{q}_{11} & 0 & 0 & 0 & 0 & \mathbf{q}_{22} & \mathbf{q}_{12} & 0 & \mathbf{q}_{23} & \mathbf{q}_{13} & 0 \\ \mathbf{q}_{31} & 0 & \mathbf{q}_{11} & 0 & 0 & 0 & \mathbf{q}_{32} & 0 & \mathbf{q}_{12} & \mathbf{q}_{33} & 0 & \mathbf{q}_{13} \\ 0 & \mathbf{q}_{31} & \mathbf{q}_{21} & 0 & 0 & 0 & 0 & \mathbf{q}_{32} & \mathbf{q}_{22} & 0 & \mathbf{q}_{33} & \mathbf{q}_{23} \end{bmatrix}. \quad (66)$$

REFERENCES

- [1] H. Deng, W. Zhang, E. Mortensen, T. Dietterich, and L. Shapiro, "Principal curvature-based region detector for object recognition," 06 2007.
- [2] D. N. Thanh, V. S. Prasath, N. N. Hien *et al.*, "Melanoma skin cancer detection method based on adaptive principal curvature, colour normalisation and feature extraction with the ABCD rule," *Journal of Digital Imaging*, vol. 33, no. 3, p. 574, 2020.
- [3] F. Mokhtarian and R. Suomela, "Robust image corner detection through curvature scale space," *IEEE Transactions on Pattern Analysis and Machine Intelligence*, vol. 20, no. 12, pp. 1376–1381, 1998.
- [4] W. Zhang, C. Sun, T. Breckon, and N. Alshammari, "Discrete curvature representations for noise robust image corner detection," *IEEE Transactions on Image Processing*, vol. 28, no. 9, pp. 4444–4459, 2019.
- [5] X. He and N. H. C. Yung, "Corner detector based on global and local curvature properties," *Optical engineering*, vol. 47, no. 5, p. 057008, 2008.
- [6] Y. Tang, H. Li, X. Sun, J.-M. Morvan, and L. Chen, "Principal curvature measures estimation and application to 3D face recognition," *J. Math. Imaging Vis.*, vol. 59, no. 2, pp. 211–233, oct 2017. [Online]. Available: <https://doi.org/10.1007/s10851-017-0728-2>
- [7] P. Fischer and T. Brox, "Image descriptors based on curvature histograms," 09 2014, pp. 239–249.
- [8] Z. QiuXiang, K. Yin, and Y. Duan, "Image reconstruction by minimizing curvatures on image surface," *Journal of Mathematical Imaging and Vision*, vol. 63, 01 2021.
- [9] Q. Zhong, Y. Li, Y. Yang, and Y. Duan, "Minimizing discrete total curvature for image processing," in *Proceedings of the IEEE/CVF Conference on Computer Vision and Pattern Recognition*, 2020, pp. 9474–9482.
- [10] S.-H. Lee and J. K. Seo, "Noise removal with Gauss curvature-driven diffusion," *IEEE Transactions on Image Processing*, vol. 14, no. 7, pp. 904–909, 2005.
- [11] S. Kim, "PDE-based image restoration: A hybrid model and color image denoising," *IEEE Transactions on Image Processing*, vol. 15, no. 5, pp. 1163–1170, 2006.
- [12] S. K. Nc and Y. Radhika, "Optimized maximum principal curvatures based segmentation of blood vessels from retinal images," *Biomedical Research-tokyo*, vol. 30, pp. 308–318, 2019. [Online]. Available: <https://api.semanticscholar.org/CorpusID:132827158>
- [13] J. E. Lutton, S. Collier, and T. Bretschneider, "A curvature-enhanced random walker segmentation method for detailed capture of 3D cell surface membranes," *IEEE Transactions on Medical Imaging*, vol. 40, no. 2, pp. 514–526, 2021.
- [14] B. Goldluecke and D. Cremers, "Introducing total curvature for image processing," in *2011 International Conference on Computer Vision*. IEEE, 2011, pp. 1267–1274.
- [15] D. Chen, J.-M. Mirebeau, and L. D. Cohen, "A new finisler minimal path model with curvature penalization for image segmentation and closed contour detection," in *Proceedings of the IEEE Conference on Computer Vision and Pattern Recognition*, 2016, pp. 355–363.
- [16] N. Y. El-Zehiry and L. Grady, "Contrast driven elastica for image segmentation," *IEEE Transactions on Image Processing*, vol. 25, no. 6, pp. 2508–2518, 2016.
- [17] R. Goldman, "Curvature formulas for implicit curves and surfaces," *Computer Aided Geometric Design*, vol. 22, no. 7, pp. 632–658, 2005, geometric Modelling and Differential Geometry. [Online]. Available: <https://www.sciencedirect.com/science/article/pii/S0167839605000737>
- [18] Gong, Yuanhao and Tang, Wenming and Zhou, Lebin and Yu, Lantao and Qiu, Guoping, "A discrete scheme for computing image's weighted gaussian curvature," in *2021 IEEE International Conference on Image Processing (ICIP)*, 2021, pp. 1919–1923.
- [19] J. E. Taylor, "II—mean curvature and weighted mean curvature," *Acta metallurgica et materialia*, vol. 40, no. 7, pp. 1475–1485, 1992.
- [20] D. Thanh, S. Dvoenko, S. Prasath, and N. Hai, "Blood vessels segmentation method for retinal fundus images based on adaptive principal curvature and image derivative operators," 05 2019.
- [21] A. Ciomaga, P. Monasse, and J.-M. Morel, "The image curvature microscope: Accurate curvature computation at subpixel resolution," *Image Processing On Line*, vol. 7, pp. 197–217, Jul. 2017. [Online]. Available: <https://hal-enpc.archives-ouvertes.fr/hal-01556888>
- [22] H.-C. Han, "Twisted blood vessels: Symptoms, etiology and biomechanical mechanisms," *Journal of vascular research*, vol. 49, pp. 185–97, 03 2012.
- [23] L. Hathout and H. M. Do, "Vascular tortuosity: A mathematical modeling perspective," *The Journal of Physiological Sciences*, vol. 62, pp. 133–145, 2012.
- [24] G. Gerig, S. Gouttard, and I. Corouge, "Analysis of brain white matter via fiber tract modeling," in *The 26th Annual International Conference of the IEEE Engineering in Medicine and Biology Society*, vol. 2. IEEE, 2004, pp. 4421–4424.
- [25] Y. Atiskova, J. Wildner, M. Spitzer, C. Aries, N. Muschol, and S. Dulz, "Retinal vessel tortuosity as a prognostic marker for disease severity in Fabry disease," *Orphanet Journal of Rare Diseases*, vol. 16, 12 2021.
- [26] E. Bullitt, G. Gerig, S. M. Pizer, W. Lin, and S. R. Aylward, "Measuring tortuosity of the intracerebral vasculature from MRA images," *IEEE transactions on medical imaging*, vol. 22, no. 9, pp. 1163–1171, 2003.
- [27] G. Choi, C. Cheng, N. Wilson, and C. Taylor, "Methods for quantifying three-dimensional deformation of arteries due to pulsatile and nonpulsatile forces: Implications for the design of stents and stent grafts," *Annals of biomedical engineering*, vol. 37, pp. 14–33, 12 2008.
- [28] L. Liu, D. Chen, M. Shu, B. Li, H. Shu, M. Paques, and L. D. Cohen, "Trajectory grouping with curvature regularization for tubular structure tracking," *IEEE Transactions on Image Processing*, vol. 31, pp. 405–418, 2021.
- [29] U. Ozertem and D. Erdogmus, "Locally defined principal curves and surfaces," *The Journal of Machine Learning Research*, vol. 12, pp. 1249–1286, 2011.
- [30] —, "Nonparametric snakes," *IEEE Transactions on Image Processing*, vol. 16, no. 9, pp. 2361–2368, 2007.
- [31] "The MNIST database of handwritten digits," <http://yann.lecun.com/exdb/mnist/>.
- [32] J. M. Brown, J. P. Campbell, A. Beers, K. Chang, S. Ostmo, R. P. Chan, J. Dy, D. Erdogmus, S. Ioannidis, J. Kalpathy-Cramer *et al.*, "Automated diagnosis of plus disease in retinopathy of prematurity using deep convolutional neural networks," *JAMA ophthalmology*, vol. 136, no. 7, pp. 803–810, 2018.
- [33] F. Cervantes-Sanchez, I. Cruz-Aceves, A. Hernandez-Aguirre, M. A. Hernandez-Gonzalez, and S. E. Solorio-Meza, "Automatic segmentation of coronary arteries in X-ray angiograms using multiscale analysis and artificial neural networks," *Applied Sciences*, vol. 9, no. 24, 2019. [Online]. Available: <https://www.mdpi.com/2076-3417/9/24/5507>
- [34] H. Li, B. Duvvuri, R. Borsoi, T. Imbiriba, E. Beighley, D. Erdoğan, and P. Closas, "Online multi-resolution fusion of space-borne multispectral images," in *2022 IEEE Aerospace Conference (AERO)*. IEEE, 2022, pp. 1–12.
- [35] A. Zeng, C. Wu, W. Xie, J. Hong, M. Huang, J. Zhuang, S. Bi, D. Pan, N. Ullah, K. N. Khan, T. Wang, Y. Shi, X. Li, G. Lin, and X. Xu, "ImageCAS: A large-scale dataset and benchmark for coronary artery segmentation based on computed tomography angiography images," *Computerized Medical Imaging and Graphics*, p. 102287, 2023. [Online]. Available: <https://www.sciencedirect.com/science/article/pii/S0895611123001052>
- [36] A. K. Jain, *Fundamentals of digital image processing*. Prentice-Hall, Inc., 1989.